Mixed Impact of Torsion on LV Hemodynamics: a CFD Study based on the Chimera Technique

Federico Canè [1e], Matteo Selmi [2,3], Gianluca De Santis [4], Alberto Redaelli [3], Patrick Segers [1], Joris Degroote [5]

1 IBiTech – bioMMeda, Department of Electronics and Information Systems, Ghent University, Ghent, Belgium

2 Division of Cardiac Surgery, Department of Surgery, Università di Verona, Verona, Italy

3 Department of Electronics, Information and Bioengineering, Politecnico di Milano, Milano, Italy

4 FEops NV, Ghent, Belgium

5 Department of Flow, Heat and Combustion Mechanics, Ghent University, Ghent, Belgium

[e] E-mail: federico.cane@ugent.be

ABSTRACT

Image-based patient-specific Computational Fluid Dynamics (CFD) models of the Left Ventricle (LV) can be used to quantify hemodynamics-based biomarkers that can support the clinicians in the early diagnosis, follow-up and treatment planning of patients, beyond the capabilities of the current imaging modalities. We propose a workflow to build patient-specific CFD models of the LV with moving boundaries based on the Chimera technique to overcome the convergence issues previously encountered by means of the Arbitrarian Lagrangian Eulerian approach. The workflow was tested while investigating whether the torsional motion has an impact on LV fluid dynamics. Starting from 3D cine MRI scans of a healthy volunteer, six cardiac cycles were simulated in three CFD LV models: with no, physiological, and exaggerated torsion. The Chimera technique was robust in handling the impulsive motion of the LV endocardium, allowing to notice cycle-to-cycle variations in every simulated case. Torsion affected slightly velocity, vorticity, WSS. It did not affect energy loss and induced a double-sided effect in terms of residence time: the particles ejected in one beat decreased, whereas the motility of the particles remaining in the LV after 2 beats was affected only in the exaggerated torsion case, indicating that is worth to include torsion in patient-specific CFD models when >25°. Nonetheless, caution is warranted when interpreting these results given the absence of the mitral valve, the papillary muscles, and the trabeculae. The effects of the mitral valve will be evaluated within an Fluid Structure Interaction simulation framework as further development of the current model.

Keywords: left ventricular torsion; Chimera technique; Overset mesh; residence time; particle tracking; CFD; patient-specific.

1. INTRODUCTION

With Cardiovascular Disease being the leading cause of death worldwide with global mortality of 31% [1], the progressive ageing of the population challenges the clinical routine, creating needs for new tools to assist the clinicians. In this regard, Computational Fluid Dynamics (CFD) modeling can provide relevant variables, such as local pressures gradients, velocities, energy indexes, residence time and shear stress, which would otherwise require invasive procedures such as catheterization [1], [2]. Furthermore, the continuous progress of computational performance (as indicated by Moore's law [3]) and medical imaging modalities opens perspectives for new concepts of diagnostics, therapy and surgical planning based on patient-specific CFD models. In comparison with cardiac in vivo imaging modalities, such as 3D ultrasound, cine-MRI and 4D flow MRI, patient-specific CFD cardiac simulations allow for a finer spatial and temporal resolution which is necessary to fully comprehend LV fluid dynamics and explore how imaging data can be converted into quantitative metrics, useful for the clinic, and with a clear mechanistic interpretation. Furthermore, such simulations also allow us to assess the impact that medical imaging protocols and subsequent image and signal processing may have on the interpretation of the measured flow field and appreciate the impact of limited resolution, averaging and filtering on the visualized flow metrics. An example is the work of Chnafa et al. [4], who demonstrated the existence of turbulence in the left ventricle using computational models, which is impossible to visualize in vivo due to the temporal and spatial limitations of all existing imaging modalities, or the work of Van Cauwenberge et al. [5]. where CFD simulations were used as the basis and ground truth of virtual ultrasound sequences of the (idealized) ventricle.

Despite the clinical application of CFD modeling in cardiology applications is still very limited, the FDA approval in 2016 of HeartFlow [6] (which diagnoses the Fractional Flow Reserve in the individual patient by means of CT images of the coronary vasculature) together with the CE mark of TAVIguide [7] (which predicts a.o. the paravalvular leakage in endovascular aortic valve treatment) demonstrate the recent breakthrough of patient-specific CFD techniques. Such level of clinical application readiness is not within immediate reach for simulations involving blood flow inside cardiac chambers. When focusing on the Left Ventricle (LV), several factors arise the complexity of the CFD problem, among which the irregularities on the endocardial surface determined by the trabeculae carneae and the papillary muscles [8]–[11], the large deformation of the LV endocardium, the

impulsive kinetics of the Mitral Valve (MV) leaflets, and the transitional-to-turbulent flow in the LV sac [4]. The combination of all these factors implies that flow should be solved as part of a CFD or a fluid-structure interaction problem where the motion and deformation of the wall and leaflets may or may not be prescribed. Even though, to the best of our knowledge, they have never been combined all together, patient-specific CFD simulations of the LV have already been used to compare the surgical options to treat patients with ventricle malformation [12], [13] and to improve our understanding of the impact of cardiac pathologies, such as dilated [14], [15] and hypertrophic [16] cardiomyopathy, and myocardial infarction [16] on intraventricular flow dynamics. As confirmed by these studies, patient-specific CFD simulations can have an important impact in several clinical applications and, in this regard, we want to improve our current level of the technology that would allow for more robust patient-specific CFD simulations of cardiac hemodynamics.

Patient-specific CFD models of the LV are typically performed by means of the Arbitrary Lagrangian Eulerian (ALE) approach or the Immersed Boundary Method (IBM). In the former, the fluid domain is represented by a volume mesh, whose interface follows the imposed kinematic motion and whose inner part undergoes remeshing in cases of large deformations. In the IBM, a LV surface mesh is embedded in a 3D static Cartesian grid and the boundary conditions are imposed by a localized body force term in the Navier-Stokes equations. The advantage is that the flow solver can be simple and fast by using a Cartesian grid, whereas the weaknesses are the loss of accuracy and smearing out near the interface caused by the interpolations [17], [18]. In previous work, our group developed a patient-specific CFD model of the Left Ventricle (LV) [19] to investigate the fluid dynamics inside the LV chamber by means of an ALE approach, taking into account both the motion of the LV and MV starting from a 4D ultrasound dataset. The method, however, remains cumbersome and convergence is not always assured, often due to negative volume errors induced by the complex and large mesh motion, resulting in simulations restricted to one cardiac cycle.

From our perspective, we can overcome these limitations using the Chimera (or overset mesh) technique, which is particularly suitable in handling problems where different components are in motion, but has not yet been widely applied to cardiovascular problems. The Chimera technique decomposes the fluid domain in overlapping fluid grids, which exchange information via interpolation of the flow variables during the calculation. The main advantage, with respect to the ALE approach, is the capability of handling the separation of the fluid domain

without requiring the local fictitious increase of viscosity or an added source term in the Navier-Stokes equations, which is a useful feature when simulating the closure of cardiac valves. With respect to the IBM, the major advantage is the possibility of representing complex geometries with boundary layer meshes [20]. On the other hand, the iterations performed between the overlapping grids to ensure that their solution is in equilibrium might increase the computational cost. In this regard, the primary aim of this study is to develop a robust workflow which allows building patient-specific CFD models based on the Chimera technique, to assess the LV fluid dynamics starting from clinical images and overcome the limitations of the previous model. This would allow us to assess also the sensitivity of calculated flow fields to the number of simulated cardiac cycles.

Furthermore, despite the main current limitations, this model can be useful to evaluate the effect that torsion may have on LV fluid dynamics. It has been shown that LV torsion is impaired or increased with cardiomyopathies, hypertrophy, diabetes, hypertension, ischemia and normal aging [21], and hypothesized that torsion is sensitive to changes in contraction and cardiac remodeling [22]. However, it is hard to assess the isolated effect of torsion from in vivo data [23], where pathology has an impact on the entire physiology of the ventricle, and not just on torsion. Torsional motion is commonly neglected in CFD models of the LV [19] and the induced effects on the LV fluid dynamics have never been investigated. Differently from Tagged MRI sequence, which evaluates the entity of the ventricular wall strain and torsion, we want to use the proposed workflow to evaluate if the impaired torsional motion can induce alterations in the fluid dynamics that could be used as biomarker to early detect pathologies. The following section reports the CFD techniques used in LV modeling, the Materials and Methods section details the steps of the workflow to build the CFD model starting from medical images [from Section 2.1 to Section 2.6] and the choice of the flow variables used to analyze the flow field [Section 2.7]. The background-overset mesh combination was determined from a mesh sensitivity analysis [Appendix]. In the Results section, we report the comparison between the considered CFD cases.

2. MATERIAL AND METHODS

The framework used to build patient-specific CFD models starting from medical images can be summarized in six steps [Figure 1], each of which is detailed in the subsections below.

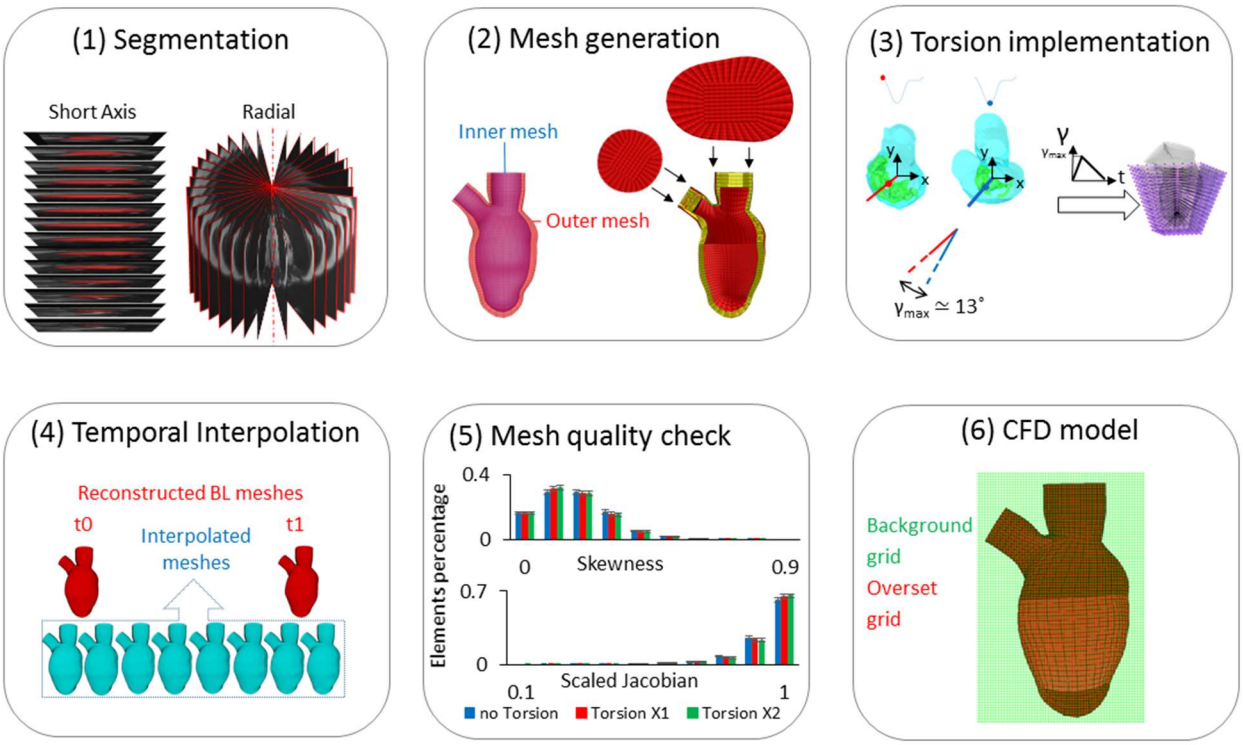

Figure 1. Workflow used to generate a patient-specific Computational Fluid Dynamics (CFD) model of the Left Ventricle (LV) based on the Chimera technique starting from medical images.

2.1 Medical Imaging Dataset Segmentation

A cine-MRI short axis dataset of a healthy male volunteer of 27 years old was manually segmented (Materialise Mimics 18.0®) to reconstruct the 4D LV endocardial surfaces in 30 time instants spanning 1 cardiac cycle. The acquisition of the medical images was performed using a Gradient Recalled Echo (GRE) sequence, with an in-plane and through-plane resolution (also known as slice thickness) of 1.17 mm and 8 mm, respectively. The study was approved by Policlinico San Donato with informed consent of the volunteer. In addition, a cine-MRI radial dataset of the same healthy volunteer was segmented (in-house Matlab-code developed by the Biomechs groups of Politecnico di Milano) to reconstruct the 4D annulus of the Mitral Valve (MV) with 18 planes rotating every 10 degrees around the axis passing

through the MV centroid and the LV apex. Also for the latter dataset, the in-plane resolution was 1.17 mm. The MV annulus was segmented from the cine-radial dataset in 30 time instants spanning one cardiac cycle. Nevertheless the motion of the MV annulus was not accounted for, it was kept in the static position obtained from averaging its 4D configurations over a cardiac cycle. The centroid of the MV annulus was computed using the built-in function in pyFormex named centroid, which returns the average coordinates of the points composing an object (curve or mesh).

2.2 Mesh generation

The Chimera technique decomposes the fluid domain in overlapping grids, in our case with (i) a fixed 3D Cartesian grid (background mesh), and (ii) a boundary layer mesh around the LV which moves and deforms every time step with the LV border and thus accounts for its motion (also called component mesh). Both meshes were generated in pyFormex, an open-source in-house python based software. The 4D boundary layer multiblock structured mesh was generated using an updated version of a previously developed semi-automatic morphing tool [25]. In the 2.0 version, the tool is applied both to the outer part of the mesh (LV endocardium) [Figure 1.2, left, in red] and to the inner one by applying a scaling factor of 0.8 [Figure 1.2, left, in blue]. Then, taking advantage of the same numbering of the nodes of the two surface meshes, the boundary layer volume meshes were created using the built-in function *Connect*, which connects the nodes of the two meshes with a number of subdivisions specified by the user. Finally, two volume plugs were built for the inlet and outlet tracts in order to have a closed boundary layer mesh.

The Cartesian background mesh was generated using a built-in function which allows the user to create a structured hexahedral mesh. The number of elements of both the component and background meshes was tuned by using the pyFormex built-in function *SubdivideIsopar*, which allows the user to divide the elements of the mesh in a defined number of sub-elements. A mesh sensitivity study

(reported in the Appendix) was conducted to choose the best combination between the density of the 4D boundary layer grid and the Cartesian one. In this study, the boundary layer mesh with 100k and 300k elements was coupled with a background mesh having an edge length of 0.5 mm and 0.7 mm.

2.3 Implementation of torsional motion

The motion of the LV endocardium can be decomposed in a perpendicular component, which determines the LV volume change, and a tangential component commonly referred to as torsion.

As our 4D boundary layer meshing method tracks the perpendicular component of the LV motion, but not the torsional one, torsion was superimposed on the perpendicular deformation. To do this, we first segmented the papillary muscles in end diastole and end systole, measured the torsional angle (gamma) as the circumferential angle enclosed by the papillary muscles centroid between end diastole and end systole. This measurement was done in the coordinate system where the mitral valve centroid is the origin; the vertical axis (z axis) points towards the apex; the y axis points towards the projection of the saddle horn at the vertical height of the origin (anterior-posterior direction); the x axis is oriented towards the posterior commissure (lateral-septal direction). Under the assumption that the shortening-elongation occurs along the defined vertical direction, the torsion has been computed as the rotation of the papillary muscles' centroid in the x-y plane. The torsional angle was found to be 13˚ in our dataset. Torsion was subsequently imposed by means of a ramp-based function not directly to our 4D boundary layer meshes, but to the two scaled copies of the mapped shape (represented in Figure 1.3 in purple) used during the mesh generation of the LV sac to project the control points and also the mesh pattern. For a more extended explanation of the role of the two scaled mapped shapes and of the controls points the reader is referred to [25].

The presented workflow was used to investigate the effects of the torsional motion on the LV fluid dynamics by comparing three CFD cases with different degrees of torsion: (i) a case which takes into account only the perpendicular component, neglecting the torsional one (No Torsion); (ii) a

physiological case which takes into account both the perpendicular and torsional component (Torsion X1); (iii) a case with a physiological perpendicular component and a torsional one multiplied with a factor 2 to enhance the differences (Torsion X2).

2.4 Temporal interpolation

The temporal resolution of our imaging dataset, which corresponds to 30 time instants spanning 1 cardiac cycle, is not sufficient in order to fulfill an adequate temporal resolution for a CFD model. Therefore, a temporal interpolation of our 4D boundary layer meshes was needed. A Natural Cubic spline was chosen as interpolator function because the C2 continuity ensures the continuity and smoothness of the volume (V) and the flow rate (Q = dV/dt) waveforms. Based on our experience, the use of a cubic Bezier spline leads to discontinuities in the flow rate curve which resulted in convergence issues of the flow solver.

2.5 Mesh quality

The errors associated with negative volumes and convergence problems experienced by Bavo et al. [19] motivated us to perform the temporal mesh interpolation prior to the CFD calculation, so that we could check the quality of the 4D boundary layer mesh in every time step before starting the set-up of the CFD model. As quality parameters both the equiangle skewness (Qeas) and the Scaled Jacobian (SJ) were evaluated with threshold values set to 0.9 (max) and 0.02 (min), respectively [26]. The mesh quality check is performed both for the mesh sensitivity study and for the case study.

2.6 CFD set-up

Our CFD model is based on the Chimera technique, referred as overset mesh approach in Fluent 18.2 software package®, in which the fluid domain is represented by one moving component boundary

layer grid embedded in a 3D Cartesian one. Once the overset boundary is defined and the overset interface is initialized, the cells of the meshes are categorized as: (i) Dead cells if they lay outside the

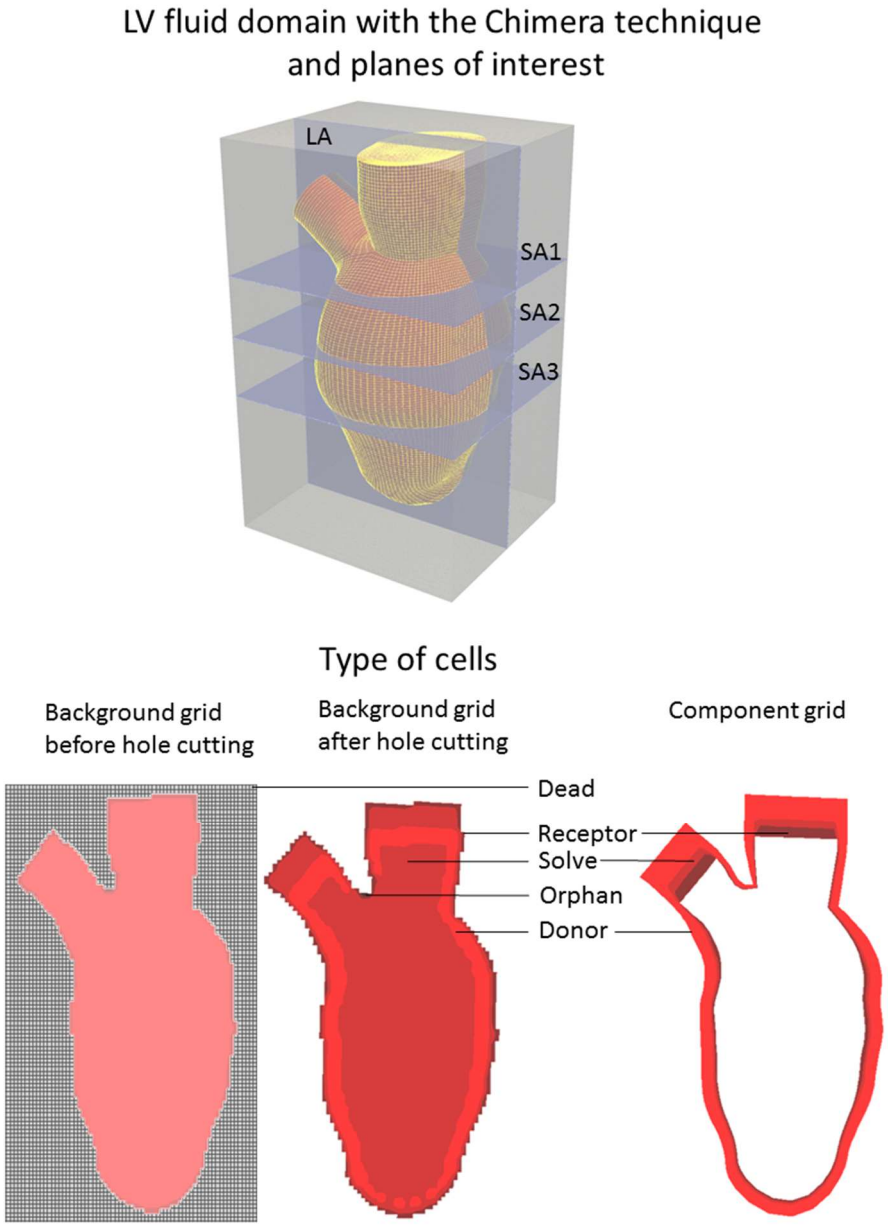

Figure 2. LV fluid domain modeling by means of the Chimera technique and location of the planes of interest (upper). Cells classification of the background and component grid for the Chimera technique in a case with meshes coarser than the ones used to show also the orphan cells (bottom).

computational fluid domain; (ii) Solve cells, in which the flow equations are solved; (iii) Receptor cells, which receive the data interpolated from the donor cells of another mesh; (iv) Donor cells, which send the data to the receptor cells and are a subset of the solve cells [Figure 2].

The following operations are automatically performed by Fluent to define the type of cells and establish the connectivity between the participating zones. Firstly, the cells lying outside the physical boundary zones of the flow region are marked as dead cells (hole cutting). Secondly, if the cells can find a suitable donor cell with higher donor priority, the solve cells are converted into receptor cells and the unnecessary receptors are turned into dead cells (overlap minimization). Lastly, the domain connectivity between solve and receptor cells is established, with each receptor that should have one solve cell (donor search). Both meshes should have at least four or more cells in the direction perpendicular to the overlap boundary in order to have sufficient overlap. In every time step, the connectivity between the zones is determined and the solver calculates the flow field by solving the Navier-Stokes equations. In terms of solver, a coupled scheme was used for the pressure-velocity coupling, while a 2^{nd} order upwind scheme was used for the convective terms and a 1^{st} order implicit scheme was used for time discretization.

Blood was modeled as a homogeneous and Newtonian ($\rho = 1060\ kg/m^3$, $\mu = 0.003\ kg/(m \cdot s)$) fluid. Due to the lack of patient-specific pressure waveforms, alternating on-off conditions were imposed at the inlet and outlet surfaces: the inlet pressure is set at 7 mmHg and the outlet is a wall during diastole, whereas the inlet becomes a wall and the outlet pressure is set at 120 mmHg during systole. Six cardiac cycles were simulated to study transient effects and cycle-to-cycle variation of the flow field and derived indices.

The simulations were run on a Dell PowerEdge R620 server (2× Intel Xeon E5-2680v2 CPUs at 2.8Ghz) using six cores, and one cardiac cycle lasted 30 hours.

2.7 Post-processing

The following variables were extracted from the simulations: velocity and vorticity magnitude along four short axis planes and one long axis plane (passing through the MV annulus centroid and the apex);

the energy loss; the Residence Time (RT) using massless ParticlePaths in the Tecplot® software environment; and the WSS distribution.

The velocity, vorticity, and WSS are compared in the end systolic configuration of every cardiac cycle, because this is the time point when the difference in the torsional angles between the simulated cases is maximal. The residence time computation is based on the last two cardiac cycles to avoid the influence of the large flow field variations that occur in the initial cardiac cycles. The stabilization effects of the numerical solution and the cycle-to-cycle variation are more extensively described in the results.

The energy loss and the energy power due to viscous dissipation was computed from the viscous portion of the incompressible Navier-Stokes equations to evaluate the influence of the different torsion degrees on the LV energetics.

To calculate RT, streamtracers are first calculated at every time step of the simulation and then used to calculate the position of massless particles, of which the paths are calculated with an integration time equal to the time step of the simulation. 4500 particles are initially placed at the starting point of each streamtracer (located in the inlet surface) and the particle positions are advanced at every time step following the streamtracers corresponding to each time level. The integration for each particle continues until the final time level is reached or until the particle leaves the solution domain. Particles are classified in three categories: (i) particles ejected within the first cardiac cycle ($0<t\leq T$); (ii) particles ejected with the second cardiac cycles ($T<t\leq 2T$); (iii) particles remaining in the LV chamber after two cardiac cycles ($t>2T$). Furthermore, we reported the particles staying inside the LV chamber after two cardiac cycles colored by the velocity magnitude and their vectors, together with their distribution in function of the velocity magnitude for the three simulated cases. Note that first and second refer to the last two cycles. As Supplementary Material, a video showing the temporal evolution of the particles

is available. The WSS distribution is reported using the bull's eye representation, which divides the LV endocardial wall into 17 sectors.

3. RESULTS

The manual segmentation of the 30 LV configurations throughout one cardiac cycle required approximately 3.5 hours and the boundary layer meshes with 1-to-1 vertex correspondence were generated within 10 minutes. The density of the component and background meshes was chosen evaluating the accuracy of four mesh combinations for the CFD case which disregards torsion. Based on the results of the mesh sensitivity analysis [Appendix], we decided to use the finest resolution for both the background (edge length = 0.5 mm) and component meshes (number of cells = 300k).

In all three simulated cases, regardless of the torsional degree, we observed a large flow field variation in the first cardiac cycle with respect to the following ones and minor cycle-to-cycle variations in the other cardiac cycles. These minor cycle-to-cycle variations affected more the shape of the patterns rather than the peak value of the investigated quantity. These transitional effects occurred in all the three simulated cases and are reported for the case with physiological torsion [Figure 3]. Because of these variations, the flow features of the three simulated cases are evaluated and compared during the last end systolic configuration.

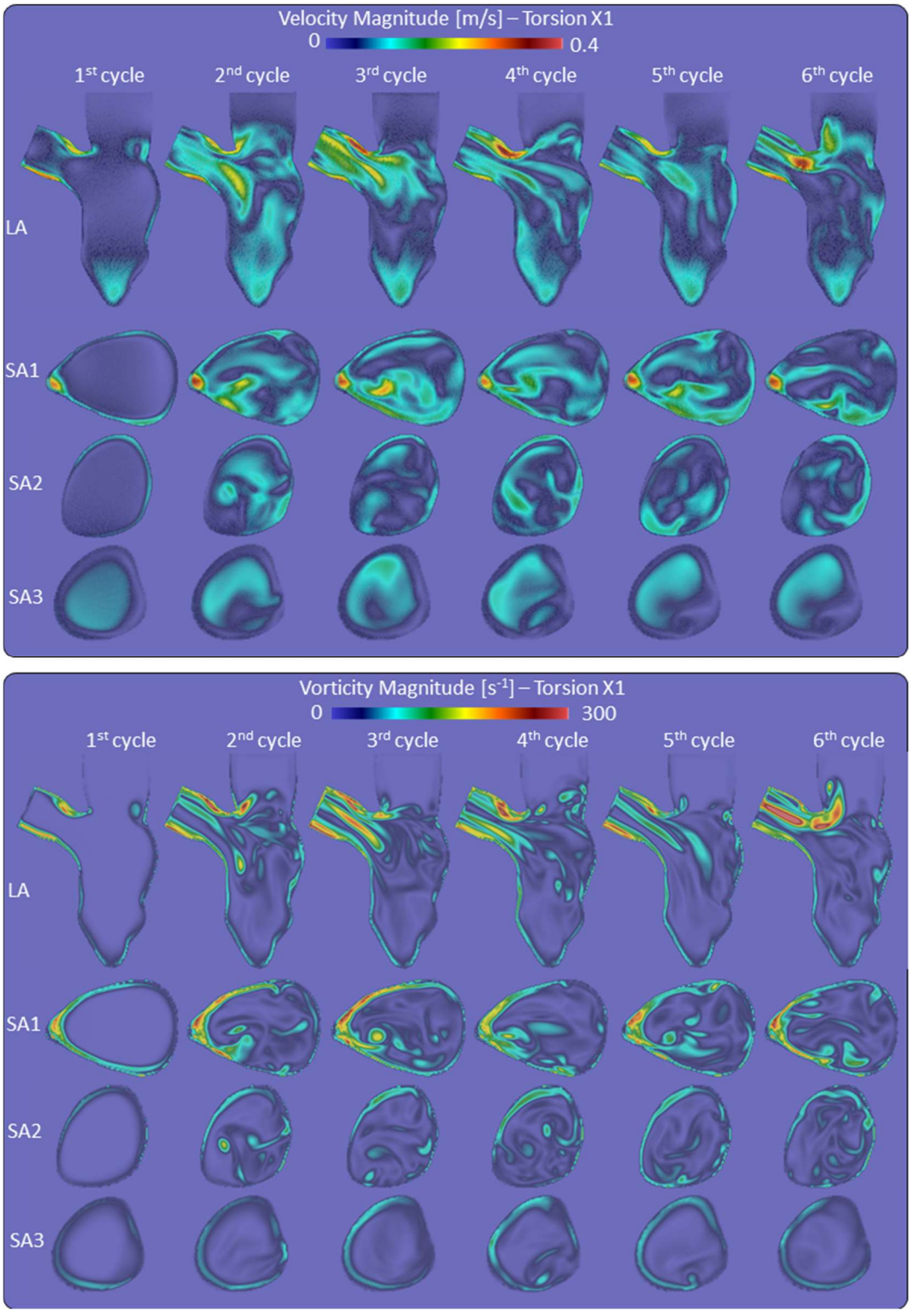

Figure 3. The cycle-to-cycle variation of velocity (upper) and vorticity (bottom) during the End Systolic (ES) configuration of the case with physiological torsion along the Long Axis (LA) plane and the three Short Axis (SA) ones. This behavior is irrespective of the torsion degree and it shows the importance of simulating at least two cardiac cycles to reach a stable solution.

Considering the velocity field, one can observe from Figure 4 that the maximum velocity in the aortic tract is located in proximity of the posterior part of the aorta wall in the Torsion X2 case, whereas in the No Torsion case it is shifted towards the anterior part of the wall (visible in the long axis view).

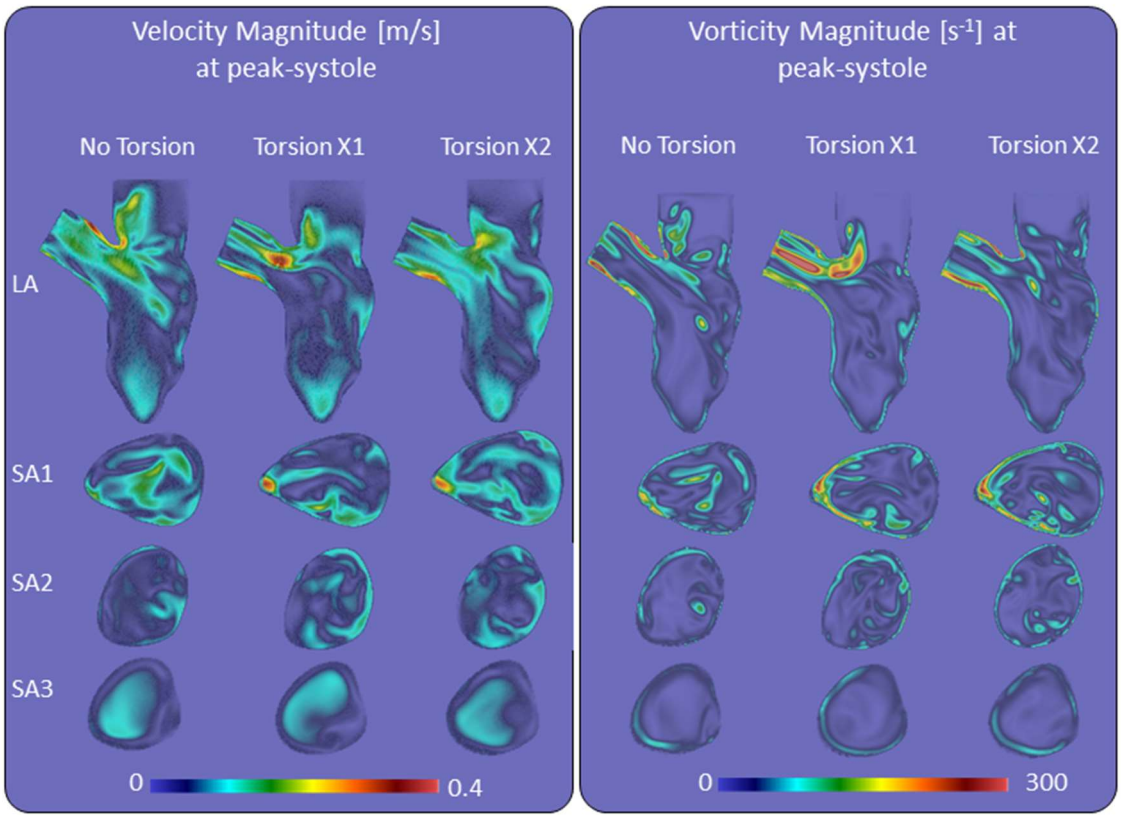

Figure 4. Velocity and vorticity in the three simulated cases to assess whether the torsion has an impact on the LV fluid dynamics. The torsional motion induces only minor differences in the extension of the spots associated with the peak values, but the maximum value of velocity and vorticity is not affected.

For the physiological case, the peak is located in the middle of the aortic lumen, which suggests that torsional motion pushes the peak located in the aortic tract towards the anterior wall. Note that only the location of the maximum value is affected, not the maximum velocity magnitude. The shift of the peak velocity value towards the outer wall is also visible in the basal short axis slice (SA1). The Torsion X2 case also shows a wider extension of the areas where velocity is above 0.1 m/s in the basal and apical planes; compared to the reference solution: +69.7%, +34.2% is found, respectively [Table 1].

		contours extension [mm^2] based on velocity range [m/s]		
		[0.0, 0.1]	[0.1, 0.2]	[0.2, 0.3]
SA1	No Torsion	655.9	529.0	1.3
	Torsion X1	945.8	309.4	11.6
	Torsion X2	728.1	536.9	7.8
SA2	No Torsion	955.9	28.2	0.0
	Torsion X1	886.7	108.5	0.0
	Torsion X2	872.5	102.3	0.0
SA3	No Torsion	501.6	156.2	0.0
	Torsion X1	548.0	110.8	0.0
	Torsion X2	510.6	148.7	0.0

Table 1. Extension of the contours [mm2] based on ranges of the velocity magnitude [m/s]. The extension of the contours with a velocity greater than 0.1 m/s increases with the torsion degree only in the medial plane.

In the medial short axis plane (SA2) the resemblance of the Torsion X2 case with the reference solution is higher than the No Torsion case: the area associated with higher velocity is more extended in both torsion cases, especially in the proximity of the endocardial wall. In the apical short axis plane (SA3) there are no significant differences between the three simulated cases.

When investigating vorticity [Figure 4 and Table 2], it is found that areas with vorticity > 200 s^{-1} increase with the torsion degree in the basal plane. This area is reduced by -71.1% for the No Torsion case, while it increases by +3% in the Torsion X2 case (in comparison to the reference case). The threshold to detect swirling patterns was set at 50 s^{-1} in the medial and apical planes because there were no areas with vorticity > 150 s^{-1}. The extension of areas with higher vorticity is reduced by -32.1% and -2.0% in the medial plane of the No Torsion and Torsion X2 case respectively, in comparison to the reference case. It increases with the torsion degree also in the apical plane: -20.1% and +7.4% in the No Torsion and Torsion X2 case respectively, in comparison to the reference case. Overall, differences are most pronounced when comparing physiological torsion with the No torsion case; the additional effect of doubling torsion on the investigated parameter is much more limited.

		contours extension [mm^2] based on vorticity range [s^{-1}]						
		[0, 50]	[50, 100]	[100, 150]	[150, 200]	[200, 250]	[250, 300]	[300, 350]
SA1	No Torsion	761.1	339.4	55.6	22.6	6.5	1.1	0.0
	Torsion X1	854.4	264.8	79.3	42.2	17.2	6.7	2.2
	Torsion X2	779.5	326.7	94.9	44.9	16.4	8.6	1.9
SA2	No Torsion	842.9	133.4	7.8	0.0	0.0	0.0	0.0
	Torsion X1	787.3	183.7	23.9	0.3	0.0	0.0	0.0
	Torsion X2	771.0	183.1	20.7	0.0	0.0	0.0	0.0
SA3	No Torsion	578.9	78.1	0.8	0.0	0.0	0.0	0.0
	Torsion X1	560.1	98.8	0.0	0.0	0.0	0.0	0.0
	Torsion X2	553.2	106.1	0.0	0.0	0.0	0.0	0.0

Table 2. Extension of the contours [mm2] based on ranges of the vorticity magnitude [s-1]. The extension of the contours with vorticity >200 s-1 and vorticity >50 s-1 increases with the torsion degree in the basal and apical planes, respectively.

The WSS does not change homogenously in all the sectors when increasing the degree of torsion. The mean WSS is proportional to the torsion degree in the basal lateral sectors and inversely proportional in the medial anterior sectors and in the apical anterior-septal sector. The maximum WSS is proportional to the torsion degree in the posterior and anterior-lateral basal sectors and inversely proportional in the posterior and septal-posterior medial sectors. In all the remaining sectors the WSS does not vary proportionally or inversely proportionally to the torsion degree.

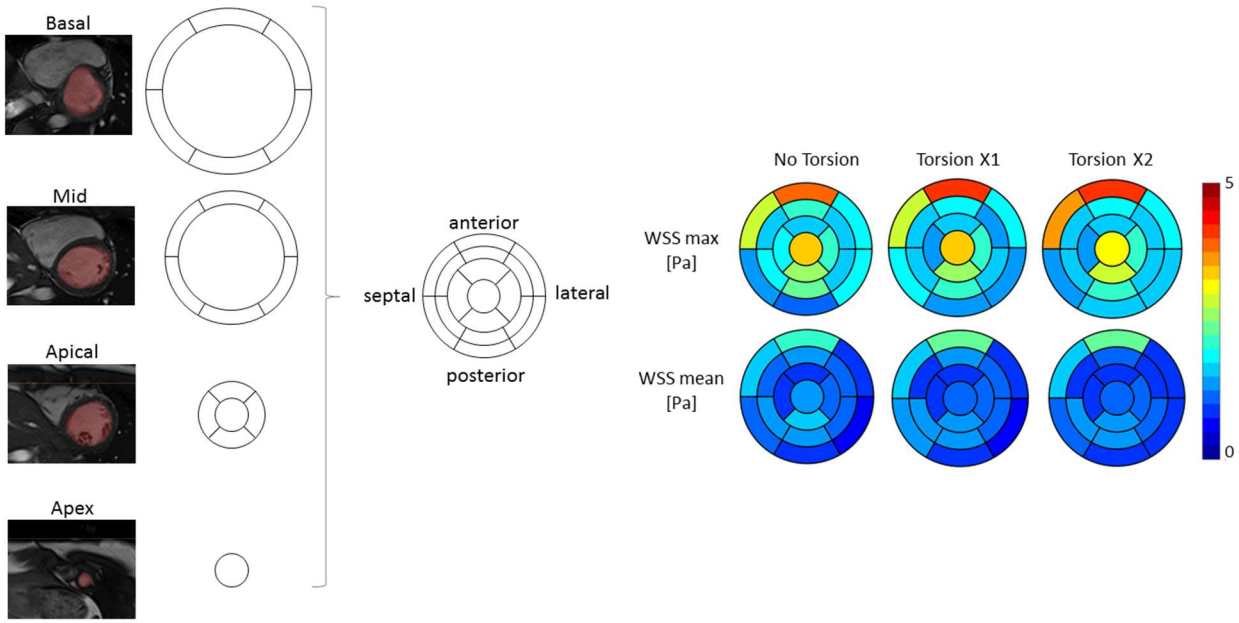

Figure 5. Corresponding Left Ventricular (LV) regions of the bull's eye model with 17 sectors, used to report the Wall Shear Stress distribution on the LV endocardium (left). Distribution of the maximum and mean WSS for the three simulated cases (right). Torsion does not induce a general homogeneous increase or decrease of the WSS.

318 The energy loss (Joule) is not affected by the different torsion degree, resulting 0.0025, 0.0024, 0.0025
319 in the No Torsion, Torsion X1 and Torsion X2 cases, respectively. This result in an average power of 1.4
320 mW in every simulated case.

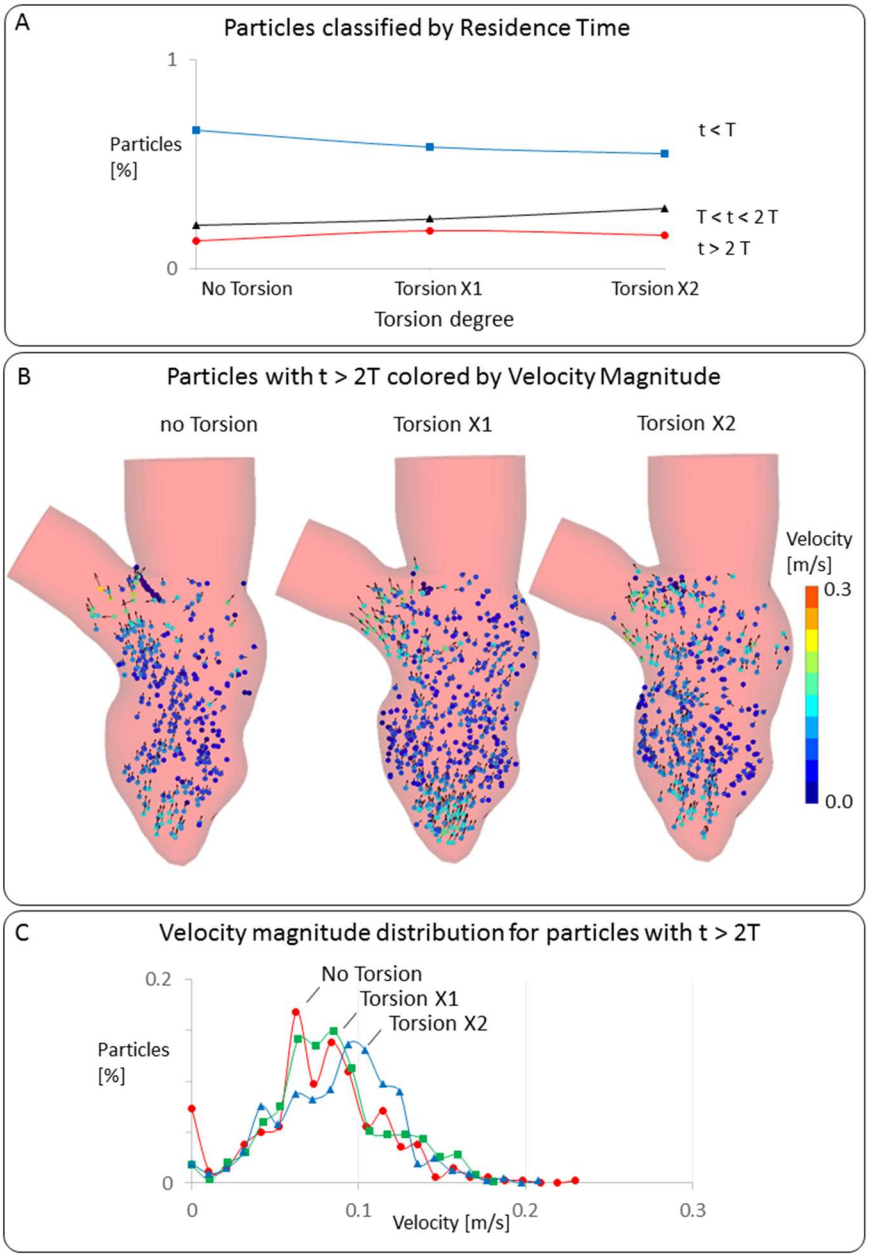

Figure 6. (A) Residence Time (RT) of the particles injected in the LV. The trend of the particles with t>2T does not increase nor decrease with the torsion degree, resulting in questions about the behavior of this class of particles. (B) The number of particles staying in the LV after two cardiac cycles is different in the three simulated cases, but no differences arise from a qualitative analysis of velocity magnitude and orientation of the vectors. (C) The distribution of the particles with t>2T in function of their velocity magnitude shows that the location of the peak value shifts towards higher velocity values by increasing the torsion degree.

321 Analyzing residence time (RT) [Figure 6], we found an increase of +7.9% of the particles with t≤T and a
322 decrease (-3.0%) of the ones with T<t≤2T for the case without torsion in comparison to the reference
323 [Figure 6.A].

Conversely, in the case with exaggerated Torsion, there is a decrease (-3.1%) of the particles with t≤T and an increase (+5.3%) of the ones residing T<t≤2T. Consequently, the number of particles residing less than 1 cardiac cycle seems to vary inversely with the imposed degree of torsion, whereas the number of particles residing T<t≤2T increases with the torsion degree. Both cases without Torsion and with Torsion X2 show a decrease of the number of particles residing more than two cardiac cycles (t>2T), -4.9% and -2.2% [Figure 6A], respectively in comparison to the reference case. The percentage of the particles with t>2T does not increase nor decrease with the torsional degree. Given that it is especially the long residing particles that are associated with an enhanced risk of thrombus formation, we focused on this class of particles. Despite that the magnitude and direction of particles velocity are comparable between the three simulated cases [Figure 6B], the quantitative analysis of the velocity distribution for the particles with t>2T added another perspective to our analysis. It is observed that the peak of the distribution of particles in function of velocity magnitude is shifted towards higher velocity values by increasing the degree of torsion [Figure 6C]. Furthermore, when categorizing the particles in three classes based on the velocity magnitude values, we found that Torsion X2 leads to more particles with velocity between 0.1 and 0.2 m/s than the other cases [Table 3], reducing the ones with velocity between 0 and 0.1 m/s.

		Velocity range [m/s]		
		[0, 0.1]	[0.1, 0.2]	[0.2, 0.3]
Particles [%]	No Torsion	75.8	23.9	0.3
	Torsion X1	74.6	25.4	0.0
	Torsion X2	60.7	39.1	0.2

Table 3. Distribution of the particles staying in the LV chamber after two cardiac cycles in function of their velocity. The case with exaggerated torsion has more particles in the velocity range between 0.1 and 0.2 m/s if compared to the other cases. This indicates that only an exaggerated torsion can enhance the motility of the particles staying the LV chamber after two cardiac cycles.

4. DISCUSSION

In this manuscript, we presented a workflow to generate patient-specific CFD models of the LV with moving boundaries based on the Chimera (or overset meshes) technique. This study is the continuation and improvement of the patient-specific LV model based on the ALE approach developed by Bavo et al. [19], which encountered frequent negative volume errors and convergence problems and, therefore, was limited to only one cardiac cycle. The advantages of the Chimera technique over the ALE and IBM approaches are reported in the section CFD approaches in lv applications. As far as we know, only Al-Azawy et al. [27] used the Chimera technique to investigate the hemodynamics in a cardiac application, a pulsatile LVAD during one cardiac cycle. In the referred case, the overset mesh approach was adopted to handle the motion of both the pusher plate and the valve: the former by defining wall velocity equations during systole and diastole, and the latter as rigid rotation. The Chimera technique was chosen to provide more insight for shear stress and strain rate near the valves. This may particularly be fundamental in biomedical cardiovascular applications where local near-wall hemodynamic factors can discern between physiological and pathological conditions at the interface between the blood and the cellular interface, affecting mass transport processes and thrombus and clots formation. The advantage of the overset mesh in handling fluid separation due to valve closure, as demonstrated in the study by Al-Azawy, is an important feature that will be useful when addressing the further development of our model, i.e., the inclusion of moving valve leaflets with valve motion obtained from fluid-structure interaction simulations.

Apart from the Chimera technique, we introduced the following modifications with respect to Bavo et al. workflow to reduce the chances of getting mesh related problems: (i) the mesh motion, as creation of the 4D meshes with nodal correspondence and their temporal interpolation, is completely handled in pyFormex with the advantage that the mesh resolution can be tuned with built-in functions and the LV kinematics is assigned in Fluent by means of customized UDFs (2.0 version of the algorithm first presented in [25]); (ii) the elimination of the spatial interpolation, needed previously to translate the

motion from the reference meshes to the mesh in Fluent, allows the user to have full control on all the nodes of the mesh; (iii) the quality check of the meshes is completely handled in pyFormex with the chance of intervening on the critical elements, if necessary, with customized scripts without manually repositioning the vertices with 3-matic; (iv) the generation of multi-block structured boundary layer meshes, with respect to tetrahedral meshes, allows to have a finer control of the mesh resolution perpendicular to the LV endocardial wall.

To test the new workflow, while also addressing a valid research question, we set up a case study to assess the impact of torsional motion on the fluid dynamics inside the left ventricle, to evaluate if patient-specific CFD modeling can be used to early detect cardiomyopathies which induce a lack of or reduction in torsion. This was accomplished by applying our framework to three CFD cases characterized by different degrees of torsional motion (i.e. a simulation without, with physiological and with amplified torsion). A mesh sensitivity study (reported in the Appendix) was performed to choose the appropriate mesh density and the coupling between background (edge length = 0.5 mm) and component grid (300k cells). The physiological torsion was measured from the cine-MRI dataset (13˚ in our dataset) and, then, it was imposed on the mapped shapes used to generate the 4D boundary layer LV meshes by means of a ramp-like function. To better understand the role of the mapped shapes the reader is referred to the paper [25]. The value of 13˚ is consistent with the one found by Conti et al. [28], which proposed a method to compute the local myocardial strains and torsion based on nearest neighbor tracking and finite-element theory.

The new workflow turned out to be effective and robust for all three CFD cases, allowing the user to overcome the convergence problems and negative volume errors encountered with the previous methodology. Thanks to the newly reached robustness, it was also possible to simulate multiple cardiac cycles, allowing us to study cycle-to-cycle variability of the calculated flow field and derived parameters.

From our CFD simulations, we observed a significant difference between the flow field of the first cardiac cycle with respect to the following ones. Even though we chose a hybrid initialization over the standard one to start with conditions closer to the real operational conditions of the LV, the differences between the first and the following cycles suggest that at least one cardiac cycle is needed to limit these transitional effects. Nonetheless, some minor cycle-to-cycle fluctuations still occur in the successive cardiac cycles, indicating that the results obtained with the previous method – in which only one cardiac cycle was simulated – need to be interpreted cautiously. Chnafa et al. [4] earlier reported these cycle-to-cycle variations of the LV fluid dynamics; in their study, 5 cycles were simulated to washout the initial conditions and results were reported based on the phase-average over 30 additional cycles. We are aware that our analysis is based on the 5^{th} and 6^{th} cycle, but limitations in computational resources prevented us to calculate more cycles. Comparing the last cardiac cycle of the three simulated cases, we noticed minor differences regarding the contours of velocity and vorticity patterns, affecting only the extension of the spots associated with the peak values but not the magnitude of the maximum values. The extension of the areas associated with velocity >0.1 m/s drops (more than 70%) in the No Torsion case in comparison to the cases with torsion in the medial plane, whereas it increases (by +69.7%, and +34.1%) in the Torsion X2 case, with respect to the reference solution, in the basal and apical plane. The vorticity magnitude decreases moving towards the apical zone in all three simulated cases. In the basal and apical plane it increases with the torsion degree whereas in the medial plane the No Torsion case is lower by more than 30% in comparison with the cases with torsion. The energy and power loss due to viscous dissipation were not affected by the different torsion degree, and resulted to be within the physiological range [29].

Several studies proposed different approaches to quantify the washout inside the left ventricle, but a direct comparison with those studies is complicated because their analysis is not based on residence time. Among these studies, Zheng et al. [30] computed the degree of mixing between atrial and ventricular blood cells and Seo et al. [31] simulated the transport and mixing of a contrast agent released in the apical region. Lastly, Selmi et al. [32] quantified the WSS at the LV apex to assess the

thrombus formation inside the LV after implantation of a left ventricular assist device, imposing both perpendicular and torsional motion components by means of customized UDF in the Fluent software environment. Of those studies allowing for a direct comparison of residence time inside the left ventricle, both Hendabadi et al. [14] and Mangual et al. [15] compared the washout of the left ventricle in patients with dilated cardiomyopathy compared to controls.

The former based the computation on Lagrangian coherent structures starting from the 2D velocity field of color-Doppler echocardiography; the latter reported a blood transit curve that measures the percentage of stroke volume ejected after a number of heartbeats. In both studies, dilated cardiomyopathy induced a delayed ejection. In Hendabadi et al., the particles with a residence time >=2 cycles are concentrated in the medial zone, similarly to the particles with $v<0.1$m/s of our simulated cases. In the study of Hendebabedi et al., the direct flow percentage of the total diastolic inflow is significantly higher in the healthy cases than the pathological cases ($P<0.01$). In Mangual et al., about 80% of the virtual tracer is ejected within two beats in the healthy cases (mean ejection fraction and stroke volume equal to 55% and 74 mL, respectively), while this value lowers to approximately 20% in the cases with DCM (mean ejection fraction and stroke volume equal to 17.8% and 41 mL, respectively). In our case study, all the three simulated cases have a percentage of direct flow comparable to the healthy cases of Mangual et al., so that the blood turnover in the cases with no and augmented torsions are not comparable with DCM cases of Mangual et al. Moreover, in our case the main difference occurs in the first systole, whereas the amount of particles ejected after two beats becomes comparable between the three cases.

To the best of our knowledge, no other studies investigated RT in the LV chamber in relation to ventricular torsion. We found that torsion reduces the number of particles staying less than 1 cardiac cycle at the expense of an increased number of particles residing in the LV with $T<t<2T$, with no significant effect of the degree of torsion on the number of particles with $t>2T$. When only considering

449 residence times, one could conclude from these data that torsion reduces the washout of the LV
450 chamber. Nevertheless, we believe that to fully understand the clinical relevance of the residence time
451 in function of the torsion degree, it is important to take into account both the number of the particles
452 remaining in the ventricle after a certain time (taken here 2 cardiac cycles) as well as their velocity
453 distribution (which may actually play a more important role in the assessment of the risk of stasis). The
454 velocity distribution between the No Torsion and Torsion X1 case is highly comparable and only the
455 Torsion X2 cases reduces the number of particles with velocity <0.1m/s, which are considered to be
456 the ones more prone to stasis [Table 3]. In a clinical scenario, the RT and the velocity distribution of
457 the particles could be used to detect the predisposition to stasis. Our data indicate that torsion will
458 have a significance only for supraphysiological values of torsion, but results should be confirmed in
459 simulations including the motion of the mitral valve leaflets. If so, the implementation of torsion could
460 be neglected when building patient-specific CFD models for cases with physiological torsion,
461 significantly reducing the complexity of the simulations. Furthermore, it is important to note that the
462 presented CFD model disregards the MV leaflets and the Trabeculae Carneae. Therefore, even though
463 our results suggest a minor impact of torsional motion on intraventricular flow, we cannot rule out
464 that the combined effect of torsion, MV kinematics and trabeculae might lead to different results,
465 particularly for the residence time. The kinematics of the MV leaflets will be evaluated as further
466 development of the current model in an FSI simulation framework.

467

5. CONCLUSION

We proposed a new robust workflow to build a patient-specific CFD model of the LV with moving boundaries based on the Chimera technique to overcome the convergence issues due to mesh-distortions of a previous model based on the ALE approach. The workflow allowed us to (i) simulate the intraventricular flow field in successive cardiac cycles and (ii) to assess whether different levels of torsion yield meaningful differences in the left intraventricular flow field. We found important transient effects on hemodynamics, implying that it is mandatory to simulate multiple cardiac cycles when addressing intraventricular hemodynamics. On the other hand, the degree of torsion was found to have a minor impact on velocity, vorticity, wall shear stress and a null impact on the energy loss. Based on our results, torsional motion in CFD modeling of the LV can be discarded for physiological torsion levels. Nonetheless, given that the current model does not include the mitral valve apparatus nor trabeculae, further model extensions are required to confirm the presented results, which at the current stage need to be interpreted with caution.

ACKNOWLEDGMENT

This work was supported by the European Commission within the Horizon 2020 Framework through the MSCA-ITN-ETN European Training Networks (project number 642458).

BIBLIOGRAPHY

[1] Y. Ishida *et al.*, “Left ventricular filling dynamics : influence of left ventricular relaxation and left atrial pressure,” *Circulation*, vol. 74, no. 1, pp. 187–196, 1986.

[2] M. Courtois, S. J. K. Jr, and P. A. Ludbrook, “Transmitral Pressure-Flow Velocity Relation Importance of Regional Pressure Gradients in the Left Ventricle During Diastole,” *Circulation*, vol. 78, no. 3, pp. 661–671, 1988.

[3] R. Mittal *et al.*, “Computational Modeling of Cardiac Hemodynamics : Current Status and Future Outlook,” *J. Comput. Phys.*, vol. 305, pp. 1065–1082, 2016.

[4] C. Chnafa, S. Mendez, and F. Nicoud, “Image-Based Simulations Show Important Flow Fluctuations in a Normal Left Ventricle: What Could be the Implications?,” *Ann. Biomed. Eng.*, vol. 44, no. 11, pp. 1–13, 2016.

[5] J. Van Cauwenberge *et al.*, “Assessing the Performance of Ultrafast Vector Flow Imaging in the Neonatal Heart via Multiphysics Modeling and In Vitro Experiments,” *IEEE Trasnsaction Ultrason. Ferroelectr. Freq. Control*, vol. 63, no. 11, pp. 1772–1785, 2016.

[6] C. A. Taylor, T. A. Fonte, J. K. Min, R. City, and L. Angeles, “Computational Fluid Dynamics Applied to Cardiac Computed Tomography for Noninvasive Quantification of Fractional Flow Reserve Scienti fi c Basis,” *J. Am. Coll. Cardiol.*, vol. 61, no. 22, 2013.

[7] M. P. De Jaegere Peter, De Santis Gianluca, Rodriguez-Olivares Ramon, Bosmans Johan, Bruining Nico, Dezutter Tim, Rahhab Zouhair, El Faquir Nahid, Collas Valérie, Bosmans Bart, Verhegghe Benedict, Ren Claire , Geleinse Marcel , Schultz Carl, Van Mieghem Nicolas, “Patient-Specific Computer Modeling to Predict Aortic Regurgitation After Transcatheter Aortic Valve Replacement,” *JACC Cardiovasc. Interv.*, vol. 9, no. 5, pp. 508–512, 2016.

[8] F. Sacco, B. Paun, O. Lehmkuhl, T. L. Iles, and P. A. Iaizzo, “Left Ventricular Trabeculations

508 Decrease the Wall Shear Stress and Increase the Intra-Ventricular Pressure Drop in CFD
509 Simulations," *Front. Physiol.*, vol. 9, no. April, p. 458, 2018.

510 [9] V. Vedula, J. H. Seo, A. C. Lardo, and R. Mittal, "Effect of trabeculae and papillary muscles on
511 the hemodynamics of the left ventricle," *Theor. Comput. Fluid Dyn.*, vol. 30, pp. 3–21, 2016.

512 [10] J. Lantz, L. Henriksson, and A. Persson, "Patient-Specific Simulation of Cardiac Blood Flow
513 From High- Resolution Computed Tomography," *J. Biomech. Eng.*, vol. 138, pp. 1–9, 2018.

514 [11] S. Kulp *et al.*, "Using High Resolution Cardiac CT Data to Model and Visualize Patient-Specific
515 Interactions between Trabeculae and Blood Flow," in *Medical Image Computing and*
516 *Computer-Assisted Intervention -- MICCAI 2011*, 2011, pp. 468–475.

517 [12] D. A. Corsini C, Baker C, Kung E, Schievano S, Arbia G, Baretta A, Biglino G, Migliavacca F,
518 Dubini G, Pennati G, Marsden A, Vignon-Clementel I, Taylor A, Hsia TY, "An integrated
519 approach to patient-specific predictive modeling for single ventricle heart palliation," *Comput.*
520 *Methods Biomech. Biomed. Engin.*, vol. 17, no. 14, pp. 1572–1589, 2014.

521 [13] E. Kung *et al.*, "Predictive modeling of the virtual Hemi-Fontan operation for second stage
522 single ventricle palliation : Two patient-specific cases," *J. Biomech.*, vol. 46, no. 2, pp. 423–
523 429, 2013.

524 [14] S. Hendabadi, R. Yotti, J. C. Del Alamo, S. Diego, and S. C. Shadden, "Topology of Blood
525 Transport in the Human Left Ventricle by Novel Processing of Doppler Echocardiography
526 Topology of Blood Transport in the Human Left Ventricle by Novel Processing of Doppler
527 Echocardiography," *Ann. Biomed. Eng.*, vol. 41, no. 12, 2013.

528 [15] J. O. Mangual *et al.*, "Comparative numerical study on left ventricular fl uid dynamics after
529 dilated cardiomyopathy," *J. Biomech.*, vol. 46, no. 10, pp. 1611–1617, 2013.

530 [16] L. Z. B. Su, J. Zhang, H. C. Tang, M. Wan, C. C. W. Lim, Y. Su, X. Zhao, R. S.Tan, "Patient-specific
531 blood flows and vortex formations in patients with hypertrophic cardiomyopathy using

computational fluid dynamics," *Biomed. Eng. Sci. (IECBES), Conf. IEEE,* vol. (Sarawak), pp. 276–280, 2014.

[17] L. Lee and R. LeVeque, "An Immersed Interface Method for Incompressible Navier-Stokes Equations," *SIAM J. Sci. Comput.*, vol. 25, no. 3, pp. 832–856, Jan. 2003.

[18] E. A. Fadlun, R. Verzicco, and P. Orlandi, "Combined Immersed-Boundary Finite-Difference Methods for Three-Dimensional Complex Flow Simulations," *J. Comput. Phys.*, vol. 161, no. 1, pp. 35–60, 2000.

[19] A. M. Bavo *et al.*, "Patient-specific CFD simulation of intraventricular haemodynamics based on 3D ultrasound imaging," *Biomed. Eng. Online*, vol. 15, no. 1, p. 107, 2016.

[20] J. R. Aarnes, T. Jin, C. Mao, N. E. L. Haugen, K. Luo, and H. I. Andersson, "Treatment of solid objects in the Pencil Code using an immersed boundary method and overset grids," *Geophys. Astrophys. Fluid Dyn.*, vol. 0, no. 0, pp. 1–23, 2018.

[21] A. A. Young and B. R. Cowan, "Evaluation of left ventricular torsion by cardiovascular magnetic resonance," *J. Cardiovasc. Magn. Reson.*, pp. 1–10, 2012.

[22] A. A. Phillips, A. T. Cote, S. S. D. Bredin, and D. E. R. Warburton, "Heart disease and left ventricular rotation – a systematic review and quantitative summary," *BioMed Cent. Cardiovasc. Disord.*, vol. 12, no. 46, 2012.

[23] C. a. Conti *et al.*, "Left ventricular modelling: a quantitative functional assessment tool based on cardiac magnetic resonance imaging," *Interface Focus*, vol. 1, no. 3, pp. 384–395, 2011.

[24] G. C. Popescu BA, Calin A, Beladan CC, Muraru D, Rosca M, Deleanu D, Lancellotti P, Antonini-Canterin F, Nicolosi GL, "Left ventricular torsional dynamics in aortic stenosis : relationship between left ventricular untwisting and filling pressures . A two- dimensional speckle tracking study †," *Eur. J. Echocardiogr.*, vol. 11, pp. 406–413, 2010.

555 [25] F. Canè *et al.*, “From 4D Medical Images (CT, MRI, and Ultrasound) to 4D Structured Mesh
556 Models of the Left Ventricular Endocardium for Patient-Specific Simulations,” *Biomed Res.*
557 *Int.*, vol. 2018, 2018.

558 [26] G. De Santis, M. De Beule, K. Van Canneyt, P. Segers, P. Verdonck, and B. Verhegghe, “Full-
559 hexahedral structured meshing for image-based computational vascular modeling,” *Med. Eng.*
560 *Phys.*, vol. 33, no. 10, pp. 1318–1325, 2011.

561 [27] M. G. Al-azawy, A. Turan, and A. Revell, “An Overset Mesh Approach for Valve Closure : An
562 LVAD Application,” *Proc. 9th Int. Jt. Conf. Biomed. Eng. Syst. Technol. (BIOSTEC 2016)*, vol. 1,
563 no. Biostec, pp. 145–151, 2016.

564 [28] C. A. Conti, E. Votta, C. Corsi, D. De Marchi, and G. Tarroni, “Left ventricular modelling : a
565 quantitative functional assessment tool based on cardiac magnetic resonance imaging,”
566 *Interface Focus*, vol. 1, no. March, pp. 384–395, 2011.

567 [29] A. J. Barker *et al.*, “Viscous Energy Loss in the Presence of Abnormal Aortic Flow,” *Magn.*
568 *Reson. Med.*, vol. 00, pp. 1–9, 2013.

569 [30] X. Zheng, J. H. Seo, V. Vedula, T. Abraham, and R. Mittal, “European Journal of Mechanics B /
570 Fluids Computational modeling and analysis of intracardiac flows in simple models of the left
571 ventricle,” *Eur. J. Mech. B/Fluids*, vol. 35, pp. 31–39, 2012.

572 [31] J. H. Seo and R. Mittal, “Effect of diastolic flow patterns on the function of the left ventricle,”
573 *Phys. Fluids*, vol. 25, no. 11, 2013.

574 [32] M. Selmi *et al.*, “Blood damage in Left Ventricular Assist Devices : Pump thrombosis or system
575 thrombosis ?,” *Int. J. Artif. Organs*, vol. 1, no. 12, 2018.

576

577

APPENDIX: Mesh sensitivity analysis

A mesh sensitivity analysis was performed to choose the best coupling between background and component mesh for our CFD case study. The background grid (bg), perfectly isotropic, is named according to the edge length, while for the component grid (cg) the number of cells is reported. Four different mesh combinations were tested (bg0.7_cg100k, bg0.7_cg300k, bg0.5_cg100k, bg0.5_cg300k) by simulating 1 cardiac cycle with a time step of 3 ms with the CFD case which disregards torsion. The following variables were investigated to compare the results of the different meshes: (i) The distribution of the mean and maximum Wall Shear Stress (WSS) during the end-systolic configuration; (ii) The 95^{th} percentile of both the WSS and the endocardial pressure during the whole cardiac cycle; (iii) Pressure and velocity along a vertical and horizontal line during the end-systolic configuration.

In order to evaluate the best mesh coupling, the finest grid combination (bg0.5_cg300k) was taken as reference solution to evaluate the studied variables [Figure 7]. In terms of WSS distribution, it is visible how the mesh combination (bg0.7_cg300k) has a closer similarity to the reference solution, suggesting that the accuracy of the WSS evaluation relies upon a finer component mesh rather than a finer background mesh. The importance of the WSS in biomedical applications to determine zones prone to thrombus formation (low WSS) and to cell damage (high WSS), would lead us to choose the finest component grid (cg300k). From the temporal evolution of the variables on the LV endocardial wall, we observed two different trends: a good match between all the meshes if considering the pressure, while from the WSS perspective once more the mesh combination (bg0.7_cg300k) has a closer similarity to the reference solution. Regarding the pressure and the velocity along lines, the mesh combination (bg0.5_cg100k) is the most similar to the reference solution in 3 out 4 cases, with the only exception being the velocity along the vertical line where the mesh combination (bg0.7_cg300k) is closer. Without having a unanimous sign that suggests the best mesh combination for all the evaluated variables, we decided to choose the finest grid combination (bg0.5_cg300k).

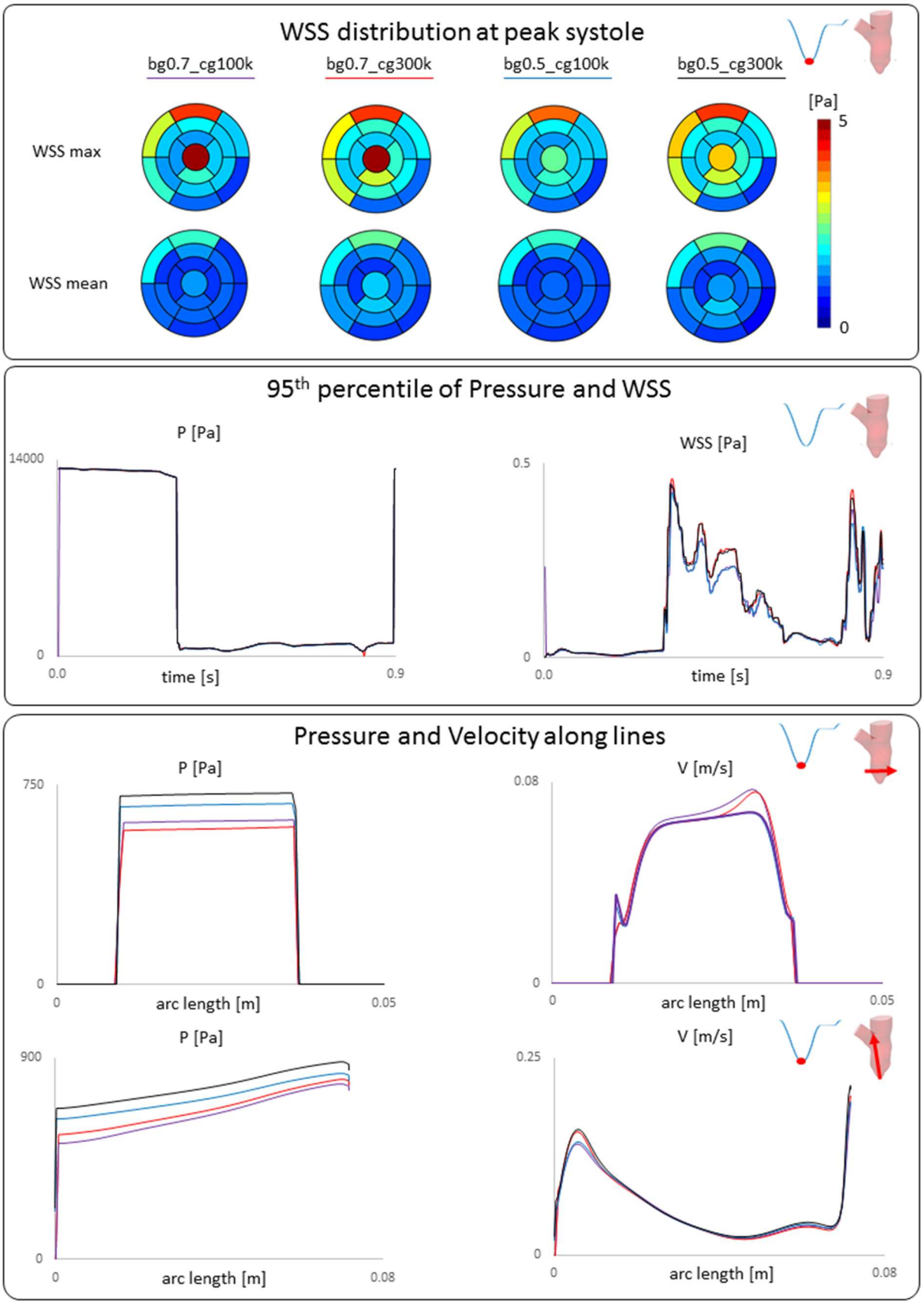

Figure 7. The mesh sensitivity study – performed on four mesh combinations – shows a different behavior for the investigated quantities. The accuracy of the WSS is affected more by the density of the component grid (cg) rather than the background grid (bg), whereas the accuracy of the quantities computed inside the fluid region (pressure and velocity) relies more on the bg. WSS and the Residence Time (which is computed from the velocity field) are equally important for our analysis, therefore we chose the mesh combination with the highest density for both the cg and bg.

603